J Neurophysiol 114: 1500–1512, 2015.
First published July 1, 2015; doi:10.1152/jn.00293.2014.

Single-unit activity, threshold crossings, and local field potentials in motor cortex differentially encode reach kinematics

Sagi Perel,[1,2] Patrick T. Sadtler,[2,3,4] Emily R. Oby,[2,3,4] Stephen I. Ryu,[6] Elizabeth C. Tyler-Kabara,[5] Aaron P. Batista,[2,3,4]* and Steven M. Chase[1,2]*

[1]*Department of Biomedical Engineering, Carnegie Mellon University, Pittsburgh, Pennsylvania;* [2]*Center for the Neural Basis of Cognition, Carnegie Mellon University, Pittsburgh, Pennsylvania;* [3]*Department of Bioengineering, University of Pittsburgh, Pittsburgh, Pennsylvania;* [4]*Systems Neuroscience Institute, University of Pittsburgh, Pittsburgh, Pennsylvania;* [5]*Department of Neurological Surgery, University of Pittsburgh, Pittsburgh, Pennsylvania; and* [6]*Department of Electrical Engineering, Stanford University, Stanford, California and the Department of Neurosurgery, Palo Alto Medical Foundation, Palo Alto, California*

Submitted 17 April 2014; accepted in final form 30 June 2015

Perel S, Sadtler PT, Oby ER, Ryu SI, Tyler-Kabara EC, Batista AP, Chase SM. Single-unit activity, threshold crossings, and local field potentials in motor cortex differentially encode reach kinematics. *J Neurophysiol* 114: 1500–1512, 2015. First published July 1, 2015; doi:10.1152/jn.00293.2014.—A diversity of signals can be recorded with extracellular electrodes. It remains unclear whether different signal types convey similar or different information and whether they capture the same or different underlying neural phenomena. Some researchers focus on spiking activity, while others examine local field potentials, and still others posit that these are fundamentally the same signals. We examined the similarities and differences in the information contained in four signal types recorded simultaneously from multielectrode arrays implanted in primary motor cortex: well-isolated action potentials from putative single units, multiunit threshold crossings, and local field potentials (LFPs) at two distinct frequency bands. We quantified the tuning of these signal types to kinematic parameters of reaching movements. We found *1*) threshold crossing activity is not a proxy for single-unit activity; *2*) when examined on individual electrodes, threshold crossing activity more closely resembles LFP activity at frequencies between 100 and 300 Hz than it does single-unit activity; *3*) when examined across multiple electrodes, threshold crossing activity and LFP integrate neural activity at different spatial scales; and *4*) LFP power in the "beta band" (between 10 and 40 Hz) is a reliable indicator of movement onset but does not encode kinematic features on an instant-by-instant basis. These results show that the diverse signals recorded from extracellular electrodes provide somewhat distinct and complementary information. It may be that these signal types arise from biological phenomena that are partially distinct. These results also have practical implications for harnessing richer signals to improve brain-machine interface control.

encoding; LFP; motor cortex; single units; threshold crossings

THE FIRST ELECTRICAL SIGNALS recorded from the brain were oscillatory in nature (Berger 1929). With the advent of sharp extracellular electrodes, action potentials from single neurons became another dominant signal source to extract information about brain function. Today, it is possible to simultaneously record single-unit activity (SUA; the times of action potentials from well-isolated neurons), threshold crossings (TCs; times when the high-band-pass-filtered voltage signal crosses a predefined threshold), and local field potentials (LFPs; low-frequency power fluctuations of the raw voltage signal). LFP signals can be further subdivided into multiple frequency bands. To maximize our ability to infer the neural basis of cognitive processes and behaviors, we should take advantage of every signal modality at our disposal. To do this, it is first necessary to establish the differences and similarities among these signal types during particular behavioral tasks.

We recorded broadband signals from multielectrode arrays implanted in primary motor cortex (M1) while two Rhesus monkeys performed a center-out reaching task. We compared the relationship to movement parameters borne by SUA, TC, and LFP in a high- and a low-frequency band that exhibited significant power modulation during our tasks. Our objectives were, first, to infer whether these signal modalities reflect the same or different information about kinematics, and second, to support the possibility of improving brain-machine interface (BMI) performance by controlling different aspects of BMI movements using different signal modalities. SUA in M1 relates to various kinematic parameters (see Riehle and Vaadia 2005 for a comprehensive review). It has been assumed that TC is a noisy proxy of SUA, conveying similar information (Fraser et al. 2009; Markowitz et al. 2011; Foster et al. 2011; Christie et al. 2014). Here, we examine this idea closely.

Previous studies have investigated the relationship between reaching kinematics and LFP (Mehring et al. 2003; Rickert et al. 2005; Asher et al. 2007; Bansal et al. 2011, 2012; Heldman et al. 2006; Zhuang et al. 2010a,2010b; Flint et al. 2012), as well as TC (Stark and Abeles 2007; Markowitz et al. 2011; Foster et al. 2011). However, SUA, TC, and LFP have seldom been directly compared in M1 recordings. Thus the important issue of differences and similarities among them cannot be firmly established based on the existing studies.

We examined each signal's encoding of four kinematic parameters: direction, position, speed, and velocity. Of these four parameters, we find find that SUA encodes direction more strongly than the other parameters, TC best encodes speed, LFP_H ("high gamma," 100–300 Hz) also best encodes speed, and LFP_L ("beta," 10–40 Hz) activity is suppressed when movement begins, but it does not bear a closer relationship to movement parameters. Thus TC appears to be more closely related to LFP_H than it is to SUA. However, we find that TC differs from LFP_H in how it is correlated across electrodes. Signals in the LFP_H band are correlated between nearby

* A. P. Batista and S. M. Chase contributed equally to this work.
Address for reprint requests and other correspondence: S. M. Chase, 4400 Fifth Ave., 115N Mellon Institute, Pittsburgh, PA 15221 (e-mail: schase@cmu.edu).

electrodes, more so than are TC signals. Taken together, our findings indicate that the four signals carry distinct information and may therefore have distinct biological origins. This implies that improved BMI performance may be achieved by extracting direction, speed, and go/no-go information from different signal sources recorded on the same sharp electrodes.

METHODS

Behavioral task. Two Rhesus monkeys performed a center-out reaching task in a two-dimensional virtual reality environment. Data analyzed here are from five sessions with *monkey J* and six sessions with *monkey L*. The animals were comfortably seated in a primate chair, in front of mirrors for reflecting a computer screen, with one arm restrained and the other free to move behind the screen. A motion-tracking system (Phasespace) was used to track the hand position in real time (resolution: 120 Hz, <1 mm). The recorded hand position was used to animate a cursor on the computer screen in real time, providing the animal feedback about the position of the hand. The workspace was a two-dimensional frontoparallel plane; the depth component of hand movements was ignored. A LabVIEW-based custom computer program controlled the behavioral task progression. At the beginning of every trial, a center target appeared and the animal had to move its hand so that the cursor location on the screen overlapped with the center target. A peripheral target appeared 200–400 ms later, cueing the animal to reach so that the cursor overlapped with the peripheral target. Successful trials ended with a water reward. If the movement took longer than 800 ms, the trial was deemed unsuccessful. Analyses were conducted using only successful trials.

A 96-electrode silicon array (Blackrock Microsystems) was chronically implanted in the arm region of the contralateral M1. Neural activity (SUA, TC, and LFP, see below) was recorded using a PZ2 system (Tucker-Davis Technologies). All procedures were approved by the University of Pittsburgh's Institutional Animal Care and Use Committee.

Neural data processing. The voltage trace recorded from each electrode was processed to obtain SUA, multiunit TCs, and LFP data. The processing steps are summarized in Fig. 1 and detailed below.

Electrode voltage signals (Fig. 1*A*) were band-pass filtered (*monkey J*: 600-6,000 Hz; *monkey L*: 300-5,000 Hz) to obtain SUA and TC signals (Fig. 1*C*). Band-pass filtering was performed using a zero-phase filter to eliminate filter delays, and edge effects were minimized by padding signals with their reflection in time. Eliminating filter delays was essential, since we compared how neural signals related to kinematics at various lags. SUA was obtained by spike-sorting the waveforms offline using either window discriminators or principal-component analysis-based clustering (custom software written in Matlab). We used a total of 122 single units in this study, combined across multiple recording sessions. TC event times were obtained using a constant threshold set at three standard deviations below the mean of the voltage trace for each channel. This technique is similar to that used in electromyography studies when relatively few motor units are present in the voltage trace (Viviani and Terzuolo 1973; Soechting et al. 1978; Burton and Onoda 1978). SUA and TC were converted to firing rates by counting TC events in 100-ms bins and dividing by the bin width. We used partially overlapping bins (50-ms overlap) to smooth the data; but results were similar with nonoverlapping bins.

Electrode voltage signals (Fig. 1*A*) were also band-pass filtered (*monkey J*: 0.3–500 Hz; *monkey L*: 10–500 Hz) and stored at a sampling frequency of 1,220 Hz to obtain LFP activity (Fig. 1*B*). The LFP power-spectral density (PSD) was computed using a 100-ms window, in steps of 50 ms and at frequency resolutions of 1 and 5 Hz (mem library from BCI2000 Project; Schalk et al. 2004). We conducted an Akaike's information criterion analysis and determined that an autoregressive model order of 30 was appropriate for our data. We verified our selection using both synthetic and real data. Results using

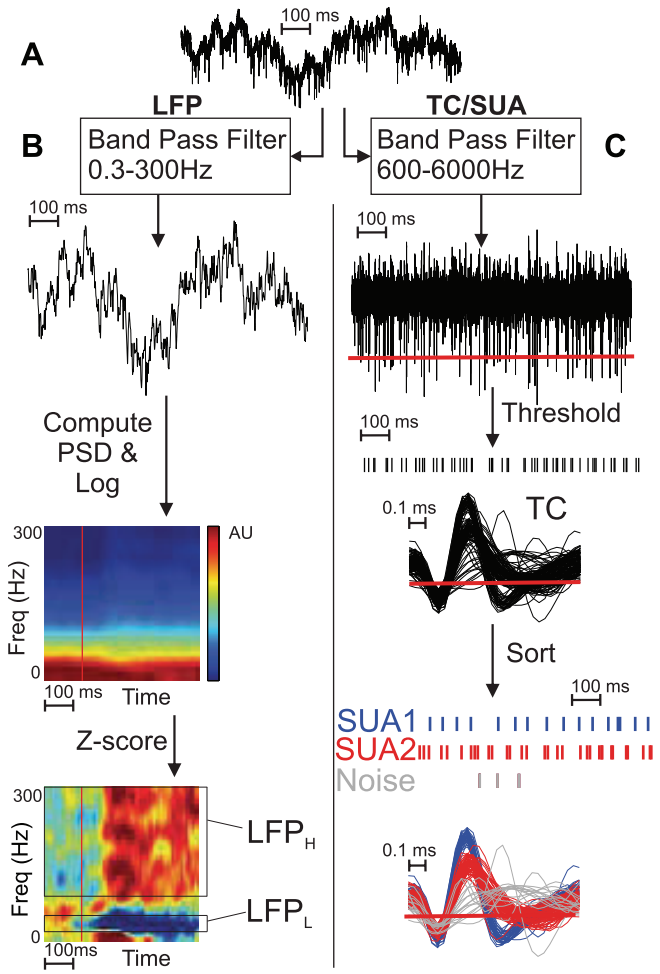

Fig. 1. Neural signal processing. *A*: raw voltage trace recorded from a single electrode. *B*: signal processing cascade for local field potentials (LFPs). Power-spectral density (PSD) is computed as a function of time and then log transformed. Separation of LFP bands is clearer when the PSD is consecutively z-scored relative to an intertrial period (Note that the PSD is only z-scored for visualization purposes). *C*: signal processing cascade for threshold crossings (TC) and single unit activity (SUA). A voltage-based threshold is used to identify TC events. TC spikes and the corresponding waveforms are shown. TC spikes are classified as either a single unit (SU) or noise. LFP_L and LFP_H, low- and high-frequency LFP.

1 Hz were similar to those using 5 Hz, and all further analyses reported here were computed at a 5-Hz frequency resolution. In our encoding analyses, we used linear regression models that make the assumption that errors are normally distributed. To match this assumption as closely as possible, we conducted all analyses on the logarithm of the LFP power values in each frequency band.

We investigated encoding of two PSD frequency bands. For *monkey J*: 15–40 Hz (LFP_L, corresponding to the "beta band" in other studies) and 100–300 Hz (LFP_H); and for *monkey L*: 15–50 Hz (LFP_L) and 100–300 Hz (LFP_H). These bands were chosen based on an examination of both single-channel and channel-averaged normalized PSD plots, since they were the bands that demonstrated similar task-related modulation. We also found that the frequency bands within the LFP_L and LFP_H bands tended to show similar encoding properties and signal correlation patterns (see Figs. 2 and 3). Because task-related modulation and regression R^2 values were significantly lower for the 40- to 90-Hz band, compared with the other frequency bands, it was not included in further analyses. Due to noise artifacts in the frequency band 28–32 Hz for *monkey J*, these frequencies were notch-filtered before computing the LFP PSD.

When averaging the PSD of individual LFP frequencies, we expect the variance of the resulting signal to behave according to the following calculation. Suppose X_1, X_2, ..., X_M represent the PSD of M individual LFP frequencies, each with variance σ^2. With the use of the variance properties $\mathrm{Var}(X + Y) = \mathrm{Var}(X) + \mathrm{Var}(Y)$ (when X, Y are independent) and $\mathrm{Var}(cX) = c^2\mathrm{Var}(X)$, a simple calculation shows that the variance of their average should be: $\mathrm{Var}([X_1 + X_2 + ... + X_M]/M) = [\mathrm{Var}(X_1) + \mathrm{Var}(X_2) + ... + \mathrm{Var}(X_M)]/M^2 = M\sigma^2/M^2 = \sigma^2/M$. Our empirical results match this theoretical calculation (see Fig. 13).

Encoding models. Many previous studies have suggested that SUA contains information about hand position, velocity, direction, and speed (for example: Moran and Schwartz 1999; Georgopoulos et al. 1986; Fu et al. 1995; Paninski et al. 2004; Paninski 2004; Riehle and Vaadia 2005). To systematically investigate how SUA, TC, and LFP relate to these kinematic parameters in our data, we regressed neural activity against kinematics and compared how well the kinematics accounted for the variance of the neural activity. We considered 4 encoding models that included 1 model per kinematic variable, and 6 additional models for certain additive combinations, for a total of 10 regression models. The four basic regression models were:

$$y = b_0 + b_{px}p_x + b_{py}p_y + noise \quad (\mathrm{P : position}) \quad (1)$$

$$y = b_0 + b_{dx}d_x + b_{dy}d_y + noise \quad (\mathrm{D : direction}) \quad (2)$$

$$y = b_0 + b_{vx}v_x + b_{vy}v_y + noise \quad (\mathrm{V : velocity}) \quad (3)$$

$$y = b_0 + b_s s + noise \quad (\mathrm{S : speed}) \quad (4)$$

where y is one of SUA firing rate (measured in spikes per second), TC firing rate (spikes per second), or LFP power (that is, log-transformed PSD, averaged across a given frequency band, as explained in RESULTS); (p_x, p_y) is the hand position; (v_x, v_y) is the hand velocity; (d_x, d_y) is the direction of hand movement; and s is the hand speed. Note that direction differs from velocity in that direction is a unit vector but the magnitude of the velocity vector is the hand's speed. The six additive combination models we tested were P + D, P + S, D + S, P + V, V + S, and P + V + S.

Signal and noise correlations. The variance of a neural signal y can be decomposed to signal and noise, where "signal" is defined as the variance explained by a set of covariates c (in our case kinematics) and "noise" is defined as the variance that remains after accounting for those covariates. This decomposition is given by the law of total variance: $\mathrm{Var}(y) = \mathrm{Var}(E(y|c)) + E[\mathrm{Var}(y|c))$, where $\mathrm{Var}(E(y|c))$ is the signal variance and $E(\mathrm{Var}(y|c))$ is the noise variance. The noise variance may be related to covariates other than the ones we included in c. From these quantities, we also computed the signal-to-noise ratio (SNR) as the ratio of the signal variance to the noise variance.

For every encoding model which used a neural signal y, we used the encoding model estimate $\hat{y}$ to calculate the signal variance as $\mathrm{Var}(E(y|c)) = \mathrm{Var}(\hat{y})$, and the residuals $y - \hat{y}$ to calculate the noise variance as $E[\mathrm{Var}(y|c)] = \mathrm{Var}(y - \hat{y})$.

Signal and noise covariance describe how two neural signals relate to a given set of covariates and are defined exactly the same way, with Cov replacing Var in the equation above. Finally, we also compute the signal and noise correlations by normalizing the signal and noise covariances by the appropriate standard deviations. Thus the signal correlation becomes $\mathrm{Cov}[E(y_1|c),E(y_2|c)]\Big/\sqrt{Var[E(y_1|c)]\times Var[E(y_2|c)]}$ and the noise correlation becomes $E[Cov(y_1|c,y_2|c)]\Big/\sqrt{E[Var(y_1|c)]\times E[Var(y_2|c)]}$. It should be noted that while the signal and average noise covariances sum to the total covariance, this does not hold true for signal and noise correlations, since they are normalized by different factors. We computed the signal covariance between pairs of neural signals, y_1 and y_2, as $\mathrm{Cov}(\hat{y}_1,\hat{y}_2)$.

Using the encoding models in the previous section, we computed the following statistics on each signal type: *1*) coefficient of determination (R^2) per electrode; *2*) SNR per electrode; *3*) signal correlation between electrodes; and *4*) noise correlation between electrodes. For LFP signals, we also computed the signal and noise covariances between individual frequency bands on the same channel and across channels. We used individual LFP PSD frequency bands from 1 to 300 Hz at a 5-Hz resolution (i.e., 1–5, 5–10, ..., 295–300 Hz).

RESULTS

Trial-averaged LFP is not representative of single-trial LFP. Previous studies related trial-averaged LFPs to kinematic parameters; hence we begin with a qualitative analysis of encoding properties of the averaged LFP signal. Figure 2 shows the time-resolved PSD for the LFP on one example electrode, averaged across repeated reaches to each peripheral target. Hand positions from representative reaches are plotted at the center, and averaged speed profiles are superimposed on the PSD plots. The LFP on this electrode appears to encode both direction and speed information. The LFP power in the high-frequency range (above ~100 Hz, $\mathrm{LFP_H}$) has a larger increase to rightward targets than in other directions. Across all reach directions, there is a tendency for the $\mathrm{LFP_H}$ power to peak just before the peak speed. The $\mathrm{LFP_L}$ band shows a clear suppression just before movement onset across all reach directions.

LFP activity during single trials is not necessarily reflective of the mean activity across trials. Figure 3 presents a comparison between trial-averaged (Fig. 3*A*) and single-trial (Fig. 3*B*) LFP PSD modulation for one example signal. While the modulation of the trial-averaged LFP power is apparent from visual inspection, it is much harder to detect a significant relationship between LFP power and kinematics in the single-trial data. This illustrates the importance of using a fine timescale when investigating in detail the properties of signals recorded from motor cortex.

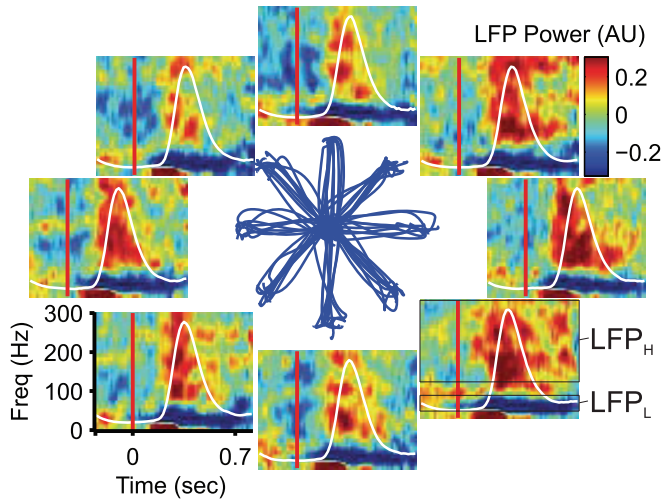

Fig. 2. Trial-averaged LFP shows both directional and speed modulation: time-frequency PSD for the LFP from 1 example electrode, averaged over repeated reaches to the 8 targets. The data are z-scored using baseline data collected between trials (not shown). The averaged hand speed profile is superimposed in white, and the go cue is indicated by a red vertical line. Hand position trajectories from 10 randomly chosen trials per target are shown at the center. This channel demonstrated simultaneous speed and directional tuning. AU, arbitrary units.

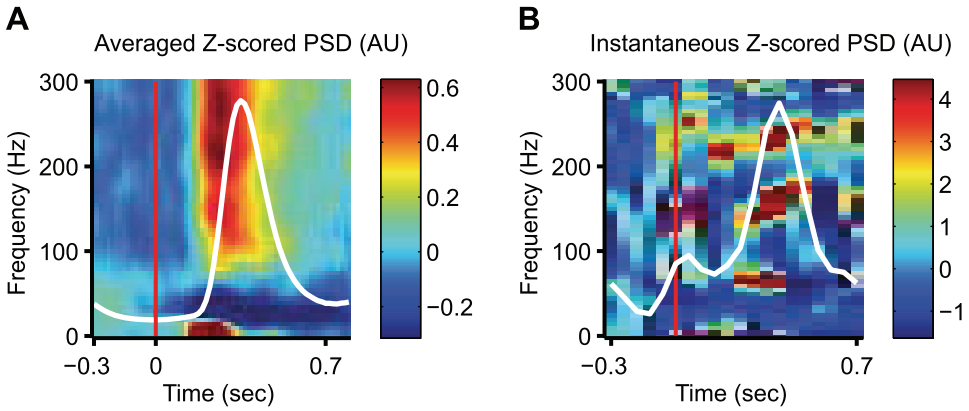

Fig. 3. Tuning of instantaneous LFP (at a resolution of 100 ms) is hard to detect visually: PSD for the LFP from 1 example electrode. *A*: PSD averaged across all trials to 2 adjacent reach targets. Speed encoding is evident by the facilitation of the LFP_H band. The averaged speed profile is superimposed in white. *B*: instantaneous PSDs for 1 of the trials (selected arbitrarily), which were used to compile the averaged PSD in *A*. Tuning is not evident in this or any other single-trial PSD.

Kinematic parameters are encoded differently among the signal types. Our next goal was to investigate how signals of each modality related to the moment-by-moment changes in kinematic parameters (neural signals and kinematics all binned at 100-ms resolution). To quantify our results, we computed the coefficient of determination (R^2) between each signal modality (SUA, TC, and both bands of LFP) and a full kinematic model consisting of position, velocity, and speed terms. We computed the R^2 at several different lags between kinematics and neural activity, ranging from −250 to 300 ms in 50-ms steps, where the negative sign indicates that neural activity precedes the kinematics. Figure 4 summarizes the resulting regression R^2 distributions across signals using data from a typical session. Figure 4, *top*, shows R^2 box plots as a function of lag, across all signals; Fig. 4, *bottom*, shows the corresponding optimal lags, defined as the lag at which the R^2 value was the highest for each channel and neural signal. Only significant regressions (determined by *F*-statistic *P* values with $\alpha = 0.05$) were included in Fig. 4, with the most common optimal lags occurring around −100 to −50 ms. The R^2 distributions across all neural modalities did not change much when evaluated at lags shifted by 50 to 100 ms backwards or forwards in time relative to the optimal lag, indicating that the regression results were not sensitive to the exact choice of a lag. We therefore chose a fixed −100-ms lag for all neural modalities in all following analyses. We also conducted analyses at lags of −150 and −50 ms. Results were similar, and thus data are shown only for the −100-ms lag.

To explore how the different neural modalities encode reach kinematics, we fit 10 regression models to every SUA, TC, and LFP signal. The regression models included one model for each kinematic parameter (position, velocity, direction, and speed) and six more models for their additive combinations (see METHODS for details). Figure 5 summarizes our findings from two representative recording sessions (with a total of 3,694 reach trials). Each box plot describes the R^2 distribution,

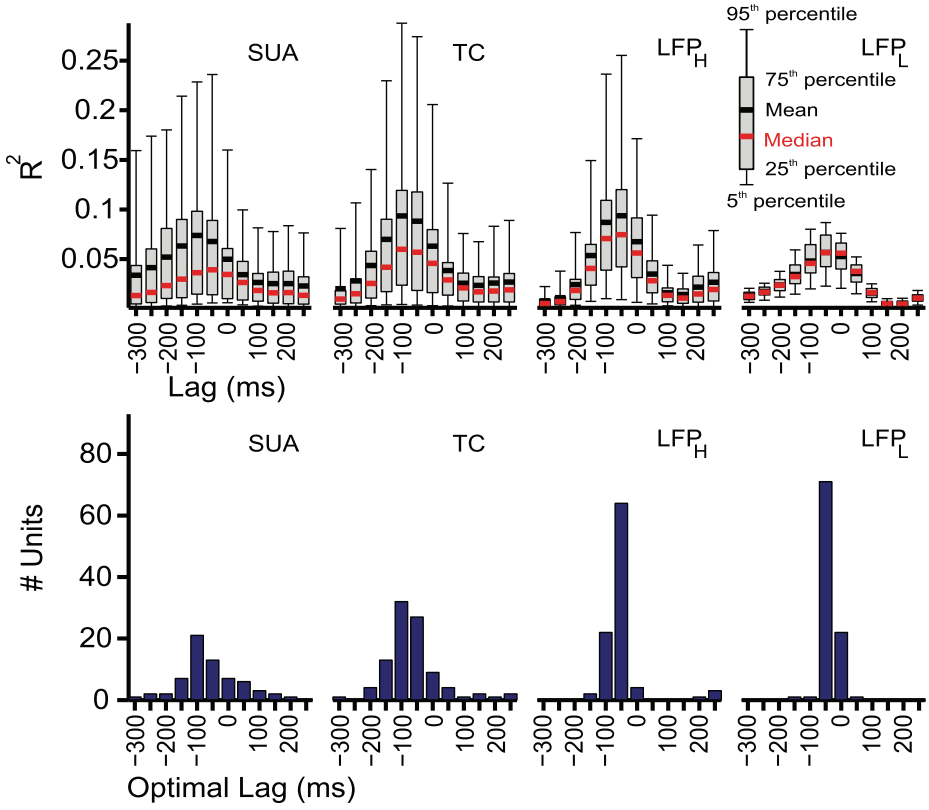

Fig. 4. *Top*: distribution of regression R^2 across lags: The full regression model (containing terms related to position, velocity, and speed) was fit using lags from −250 to 300-ms at 50-ms steps, to every neural signal modality (SUA, TC, LFP_H, and LFP_L). The box plots summarize R^2 values across all cases with significant regressions. The highest mean population R^2 values for all neural modalities are for causal lags in the range of (−50)-(−150)ms. R^2 values are the lowest for the LFP_L band, indicating it is not tuned to these kinematic variables. The box plots describe the 5, 25, 75, and 95th R^2 percentiles, as well as the mean (black) and median (red) R^2 values. *Bottom*: optimal lag histograms: distribution of lags at which maximal R^2 values occurred for every neural signal modality. Optimal lags for SUA, TC, and LFP_H are similar, although LFP_H optimal lags are more homogeneous across signals.

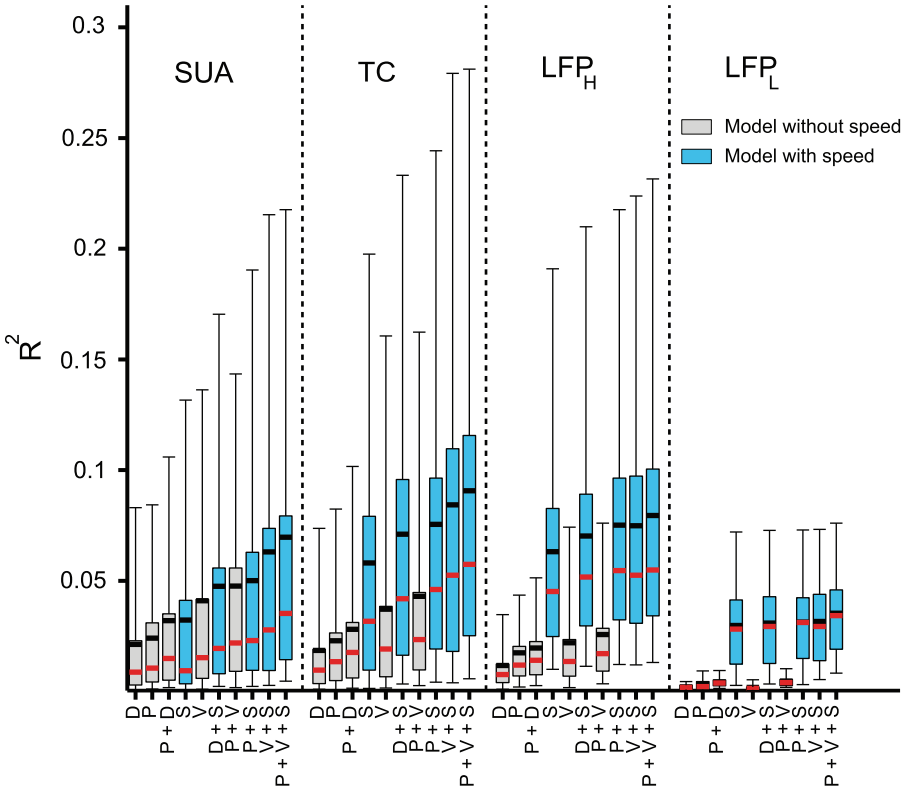

Fig. 5. Distribution of regression R^2 values across regression models: All regression models (see METHODS) were fit to all neural signals, using a fixed causal (−100-ms) lag (that is, neural data precedes kinematics). Regression models included position (P), velocity (V), direction (D), and speed (S); or their additive combinations, e.g., P + V + S, represent a model that additively includes position, velocity, and speed. All box plots for every neural modality are sorted by the SUA mean R^2 values.

across all channels, grouped by neural signal modality and organized by regression model, allowing comparisons of the types of information encoded by the different neural modalities. It should be noted that the R^2 values in Fig. 5 are lower than we observed with averaged data, because we used single-trial data at 100-ms resolution. The 10 encoding models we considered are ordered on the *x*-axis of Fig. 5 according to their mean R^2 for the SUA data; that ordering is preserved for the other three signal modalities to aid visual comparison.

Six trends are evident. *1*) In agreement with previously published results, SUA signals encode all kinematic parameters, with the highest R^2 for velocity, followed by speed, position, and direction. *2*) All signal modalities exhibit a pronounced improvement in model fit when speed is added to the model (box plots for models including speed are colored blue in Fig. 5). *3*) Based on the ordering and magnitude of the model fits, TC more closely resembles LFP_H than SUA. Indeed, when we compared the R^2 distributions for the full model (position, velocity, and speed) across SUA, TC, and LFP_H, visual inspection of the quantile-quantile plots showed that the TC R^2 distribution was more similar to the LFP_H distribution than to the SUA distribution: a two-sample Kolmogorov-Smirnov test showed that the TC R^2 distribution was significantly different from the SUA distribution ($P = 0.008$), but not significantly different from the LFP_H distribution ($P = 0.06$). *4*) TCs signals provide the best encoding among the four signal modalities, at least when speed is included in the model. *5*) LFP_L provides the poorest encoding. Finally, *6*) most of these distributions exhibit long tails and have means that are higher than medians. This indicates that a subset of channels (~20%) provide the best encoding of kinematics.

Figure 6 displays the same R^2 distribution box plots, now grouped by model type and organized by signal modality. We wish to highlight two trends evident in the data when viewed in this manner. First, for the position, direction, and velocity models, the mean R^2 was highest for SUA and decreased in this order: TC to LFP_H then LFP_L. The median R^2 showed a different trend, and this difference between mean and median indicates that the SUA R^2 distributions are skewed in the positive direction compared with TC and LFP_H. In other words, the top 25% of single units have higher R^2 compared with the top 25% of TC or LFP_H signals and therefore encode kinematics better. Second, the speed model showed a different trend, with the best encoding for LFP_H (judged by either mean or median), with TC a close second, and both SUA and LFP_L showing poorer encoding of speed. These trends were quantified using Kolmogorov-Smirnov tests: SUA and TC R^2 distributions for position, direction, and velocity models were not significantly different ($P = 0.26$, 0.12, and 0.62); but both were significantly different from the LFP_H distributions ($P = 0.003$, 0.007, and 0.001) and had higher means than the means for LFP_H signals. In contrast, mean R^2 values for the speed model increased from SUA to TC and LFP_H, and comparison of the R^2 distributions of the speed model across all neural modalities showed statistically significant differences.

To study if SUA, TC, and LFP_H encode the same directional information, we compared their preferred directions (PDs). We used the full model (position, velocity, and speed) to account for the prominent speed encoding present in all neural modalities. We estimated PDs by normalizing the velocity coefficients (b_{vx}, b_{vy}) and representing this vector as an angle around the unit circle (between −180 and +180°). Figure 7, *diagonal plots*, shows the estimated PDs for SUA, TC, and LFP_H, with one radial line for each channel. PD grey scale intensities vary by the regression R^2 values from light gray (low R^2) to black (high R^2). Figure 7, *bottom triangular portion*, compares the

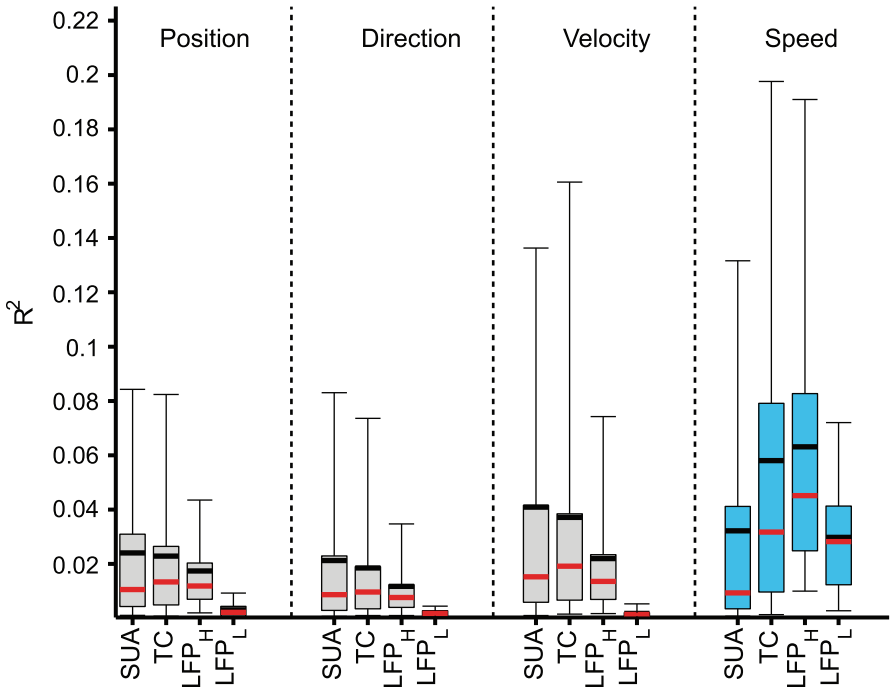

Fig. 6. Distribution of regression R^2 values across neural modalities: Four regression models were fit to all neural modalities: position (P), direction (D), velocity (V) and speed (S). The data from Fig. 5 are replotted here but now grouped by model type rather than signal modality. Position, direction, and velocity information decreases across the neural modalities (SUA $\approx$ TC $>$ LFP_H). Speed information increases across neural modalities (SUA $<$ TC $<$ LFP_H).

similarity of PDs for the different signal modalities. It contains scatter plots of PDs for different neural modalities on the same electrodes. To allow proper comparisons, we wrapped the PDs so that every data point lies as close to the equality line as possible, and therefore, some PDs extend beyond the -180 to $+180°$ range. These scatter plots demonstrate that TC PDs are better correlated with LFP_H PDs ($\rho = 0.77$) than with SUA PDs ($\rho = 0.41$). A comparison of the regression R^2 from which PDs were estimated can be found in Fig. 7, *top triangular portion*. These demonstrate that TC regression R^2 are better correlated with LFP_H R^2 ($\rho = 0.79$) than with SUA R^2 ($\rho = 0.35$).

The signal types are correlated differently across cortical tissue. We examined how different signal types were organized across the cortical tissue. To do this, we computed the correlation between signals across electrodes. Figure 8 shows histograms for correlations computed for all pairs of SUA-LFP_H and TC-LFP_H originating from the same electrode. The mean

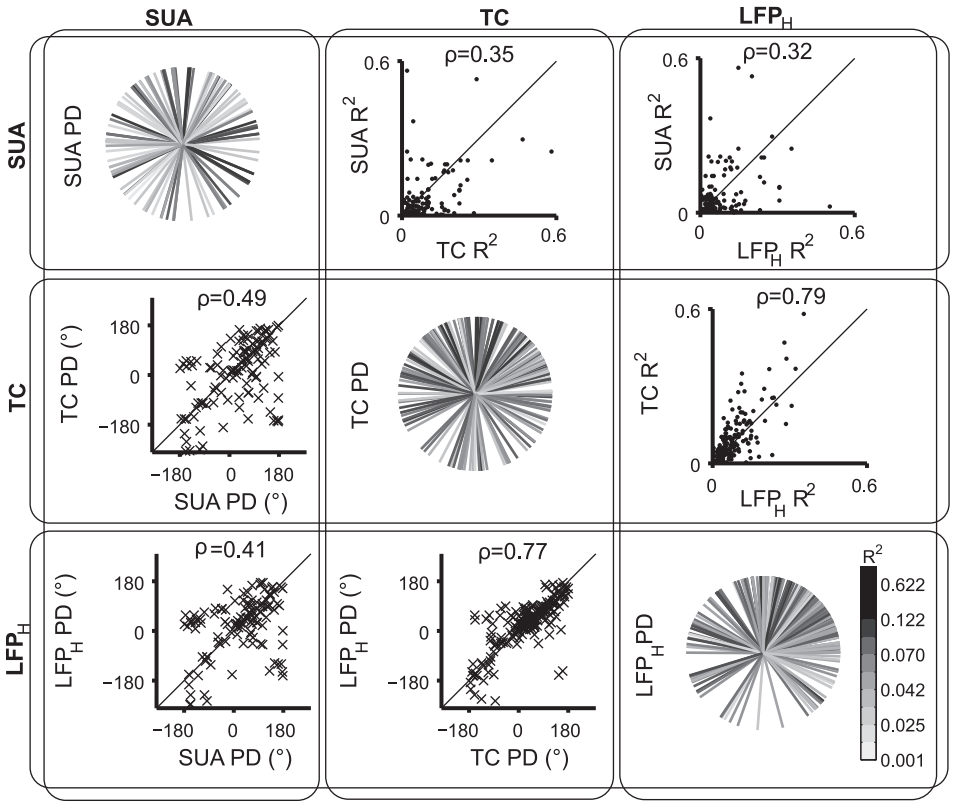

Fig. 7. Comparison of preferred directions (PDs) and R^2 between neural signals on the same channels. *Diagonal*: PDs for SUA, TC, and LFP_H signals. *Right top half*: Comparison of regression R^2 between neural signals. *Left bottom half*: Comparison of PDs between neural signals. The correlation coefficients between the R^2 and PDs are shown at the *top* of every plot.

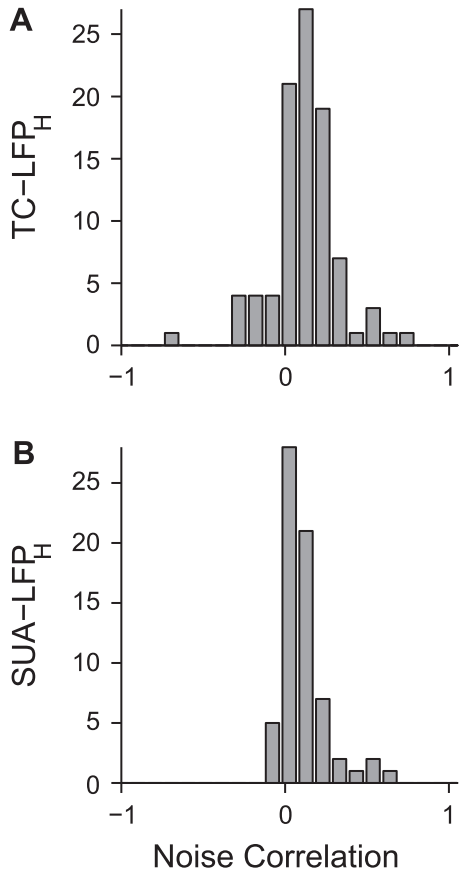

Fig. 8. SUA and TC signals show different noise correlations with LFP_H signals on the same electrode: Histograms of noise correlations between TC and LFP_H signals (*A*) and SUA and LFP_H signals (*B*). All signal pairs originated on the same electrode. Correlations were computed using the full model that included position, velocity, and speed. The mean noise correlation for SUA-LFP_H was smaller than the mean TC-LFP_H noise correlation but not significantly different.

noise correlation for SUA-LFP_H pairs was smaller than for TC-LFP_H pairs but not significantly different.

To understand the spatial integration properties of our signals, we examined the signal and noise correlations between similar modalities recorded on all pairs of electrodes across the recording array. Figure 9 shows the signal and noise correlations for all TC and LFP_H signal pairs. Every color matrix contains all correlations (either noise in Fig. 9*A* or signal in Fig. 9, *B* and *C*) between all pairs of signals on the array, sorted by their distances from one of the array corners. We observed that LFP_H recordings have higher noise correlation than do TC recordings. Because most signal types encode speed in a positive-going manner (i.e., increases in speed tend to lead to increased SUA, TC, and LFP_H activity), we computed signal correlations for models with speed (P + V + S) as well as for models without speed (P + V). With the use of a position and velocity only encoding model, LFP_H pairs also show higher signal correlation compared with TC pairs (Fig. 9*B*). TC pairs show a more heterogeneous correlation pattern compared with LFP_H pairs. That trend is even stronger when speed is added to the encoding model (Fig. 9*C*), as the LFP_H signal correlation map becomes even more uniform.

We extended our spatial correlation analysis to all LFP frequencies between 1 and 300 Hz. Results are shown in Fig. 10. We computed the signal and noise correlations between all pairs of electrodes for each frequency band. Instead of displaying one color matrix per frequency band, we summarize the data with one curve for every frequency band. Each point on a curve represents the average correlation between all electrodes that are at a certain distance from each other. Correlation strength is inversely related to frequency: correlations are strong at low frequencies and weaken as the frequency increases. Noise correlations decay with distance, while signal correlations do not.

Figure 10 shows that TC noise correlation is very low (<0.1), while noise correlations for all frequencies in LFP_H (100–300 Hz) range from 0.1 to 0.4. Signal correlations for TC are also low (0.2), compared with 0.3 to 0.8 for LFP_H frequencies. TC signal and noise correlations are as low as or lower than the ones for the highest LFP frequency we examined (290–300 Hz). We further evaluated the fidelity of encoding by SUA, TC, and LFP_H on the same electrode by quantifying the SNR of the full linear model fit (P + V + S). These SNR values are plotted against one another in Fig. 11. We found that 92% of TC and 77% of SUA signals showed better SNR than the LFP_H signals on the same electrode. More TC signals have better SNR compared with SUA signals due to the more robust TC speed encoding. It is also important to note that for all signal modalities, noise variance was much higher than signal variance. The mean ($\pm$SE) percentages of noise variance out of the total variance were 93 $\pm$ 0.8% for SUA, 92 $\pm$ 0.6% for TC and 93 $\pm$ 0.4% for LFP_H.

LFP can be averaged across frequencies to improve SNR. Because trial-averaged LFPs usually exhibit correlated modulations in neighboring frequency bands (see Fig. 3*A*), it is common practice to average the LFP across frequencies, presumably to smooth and "clean" the signal. Single-trial LFPs appear by eye to be more heterogeneous across frequency than trial-averaged LFPs (e.g., Fig. 3*B*). We examined whether LFP should be averaged across frequency bands. Averaging LFP across frequency bands would only be beneficial if those frequency bands encoded similar information but did not have correlated noise. We computed the signal and noise correlation between individual frequency bands of every LFP signal. For this analysis we used the position-velocity (P + V) encoding model and data from an entire session. We show an example of correlations for a typical electrode in Fig. 12. It is clear that noise is mostly independent across frequencies, exhibiting weak correlation for frequency bands >10 Hz apart. On the other hand, the signal correlation is high across the two frequency bands we used in this study: LFP_L (15–40 Hz) and LFP_H (100- 300 Hz). These results indicate that it should be beneficial to average single-trial LFP across these two frequency bands, rather than treat all frequency bands independently when studying how kinematic information is encoded in cortex.

If averaging across frequency bins boosts signal, then averaging the LFP across several 10-Hz frequency bins will show an enhanced SNR compared with the 10-Hz bins taken individually. We tested this separately for the LFP_L and LFP_H bands (Fig. 13). In the LFP_H band, averaging the LFP power across frequency bins before computing the SNR (ordinate) yields higher values than computing the SNR in each frequency bin first and then averaging (abscissa), by roughly a factor of $\sqrt{21}$ (the square root of the

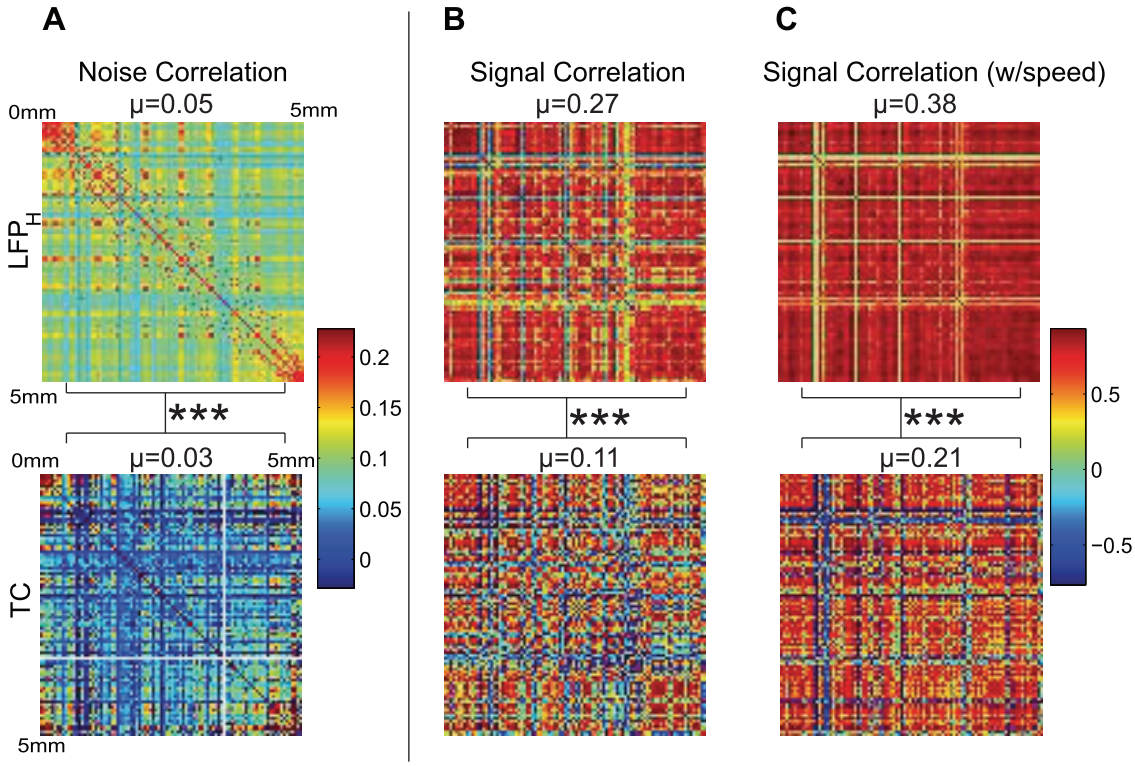

Fig. 9. LFP_H signals show different signal and noise correlation population patterns compared with TC signals: In all *A–C*, signals are ordered according to their distance from the *left-top* electrode in the array. Their distances from that electrode are indicated on the noise correlation matrices. Both noise and signal correlation were computed for every pair of signals (within the same modality) across the recording array. The average correlation across all pairs is indicated above the color matrices by μ. *A*: noise correlations between all pairs of LFP_H signals (*top*) and TC signals (*bottom*). LFP_H signals have higher noise correlation compared with TC signals. *B*: signal correlations for a position and velocity model between all pairs of LFP_H signals and TC signals. LFP_H signals have more homogeneous signal correlation compared with TC signals. *C*: same as *B* but signal correlation is computed for a position, velocity, and speed model. LFP_H signal correlations are dominated by speed, as indicated by the more homogeneous colors, but this is less true for TC signal correlations. *t*-Tests showed that in *A–C*, the top triangular values from the LFP_H and TC matrices are statistically significantly different ($P < 10^{-10}$). There is no evident spatial organization in *A–C*.

number of frequencies in LFP_H). When we repeated this analysis at 5-Hz resolution, the SNR of the average band did not continue to improve at the same rate (data not shown). This indicates that in the frequency range of LFP_H neural noise is correlated at frequency bins <10 Hz and becomes more independent at frequency bins of 10 Hz or wider. For the LFP_L band, averaging across frequency bins did not boost the signal as much. Inspection of the data indicate this is primarily because there is some heterogeneity in the LFP_L band edges: while many (~40%) channels exhibit common signal modulation from 10 to 40 Hz, in other channels these edges are slightly higher or lower. The LFP_L band heterogeneity is interesting, but due to its relatively poor kinematic encoding, we did not pursue it further here.

DISCUSSION

Our ability to simultaneously record the activity of single neurons has increased steadily with time (Stevenson and Kording 2011) and multielectrode recording arrays currently allows us to record from several hundred neurons at the same time (Collinger et al. 2013; Ifft et al. 2013; Schwarz et al. 2014). However, this still only represents a small fraction of the total number of neurons in any given brain area. We are far from the

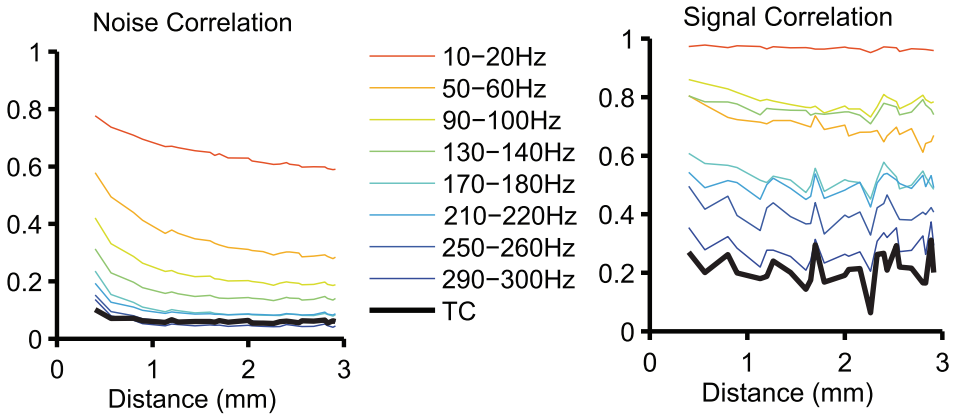

Fig. 10. Noise correlations decay with distance at a higher rate for higher frequencies. Signal correlations depend on frequency but not distance. Signal and noise correlation were computed between all pairs of signals on the array and were grouped as function of distance. The average signal and noise correlations at a certain distance are shown for different frequency bands. Both signal and noise correlations decrease the higher the frequency. Noise correlations also decay with distance. TC signal and noise correlations are lower than the ones for the highest LFP frequency band (290–300 Hz).

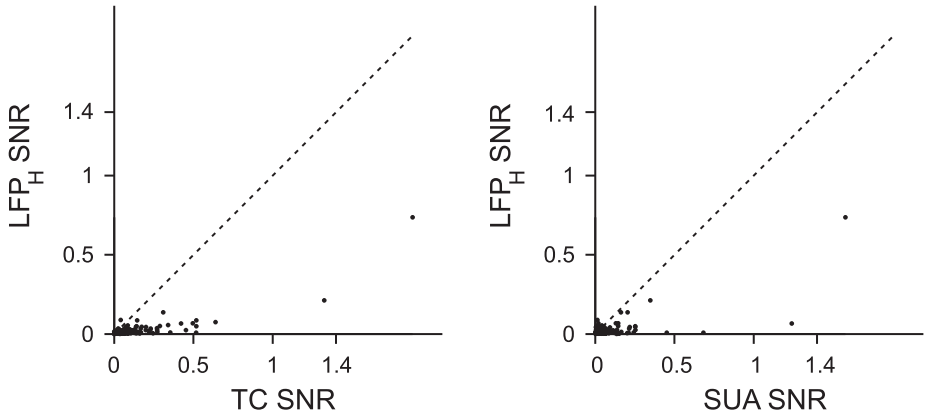

Fig. 11. SUA and TC signals have higher signal-to-noise ratio (SNR) compared with LFP_H signals. SNR comparison between SUA/TC and LFP_H signals on the same channels for the P + V + S model: 95 (77%) SUA signals show better SNR compared with LFP_H signals; 177 (92%) TC signals show better SNR compared with LFP_H signals. This difference is likely due to the more robust speed encoding in TC compared to SUA.

ultimate goal of recording from all the neurons in a complete mammalian neural circuit (Insel et al. 2013). It is therefore of critical importance to extract as much information as possible using the available recording resources.

Extracellular electrodes inserted in the cerebral cortex measure a voltage signal composed of spikes and dendritic potentials. Some spikes are large, originating from larger neurons that are close to the electrode tip, and are easily discriminated as SUA. Smaller neurons, and neurons further away from the electrode tip, contribute smaller spikes which are harder to discriminate and are commonly analyzed together as multiunit activity. In our data, TCs surely included contributions from well-isolated single neurons, nonisolatable multiunit activity, and fluctuations that could not be clearly identified as multiunit activity. Dendritic potentials likely also contribute to the voltage trace, mostly at low frequencies (Buzsáki et al. 2012). Our goal was to characterize the differences and similarities between signals that can be extracted from the extracellular voltage trace during a behavioral task. In this discussion, we focus on the implications of our results for our understanding of encoding (that is, the native tuning properties of primary motor cortex), the biological underpinnings of extracellular voltage signals, and decoding (that is, the use of motor cortex signals for BMI control).

Kinematic parameters in M1 are encoded differently by different neural signal modalities. We compared the encoding properties of three types of signals commonly extracted from intracortical electrode recordings in M1: SUA, TC activity, and LFP activity in two distinct frequency bands. To investigate how they represent kinematic parameters on a moment by moment basis, we fit a set of encoding models that included the hand's position, direction, velocity, speed, and their additive combinations. We fit these models to single-trial neural and kinematic data binned at 100-ms resolution.

We observed a progression in the encoding properties from SUA through TC to LFP_H (100–300 Hz), with directional signals showing stronger encoding among the single units and speed signals showing stronger encoding in LFP_H. SUA is the only modality for which the median R^2 for velocity was larger than the median R^2 for speed. Of all the signal types we considered, LFP_H shows the strongest encoding of speed relative to velocity. TC is intermediate between these two. Progressing from SUA through TC to LFP_H, the median R^2 for all models that include directional signals (velocity, direction, and position) shows a gradual decrease, while the median R^2 for models that include speed shows a gradual increase. For all signal modalities, the majority of the information about any particular kinematic feature is best represented by a relatively

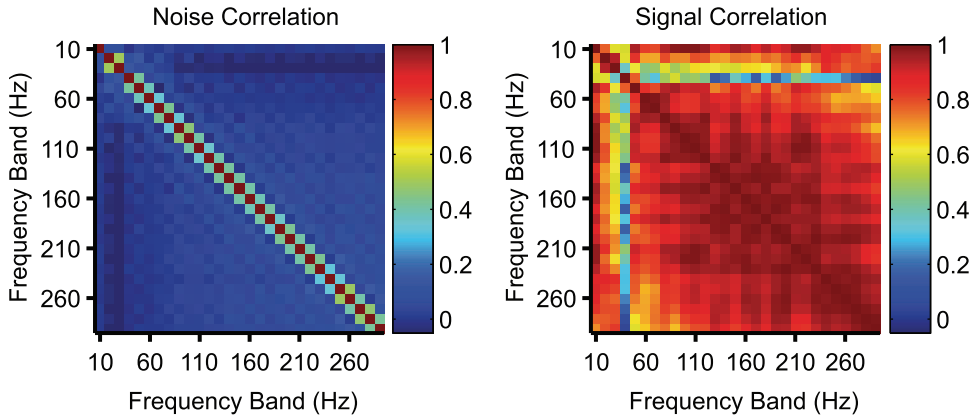

Fig. 12. Signal, but not noise, is correlated across single LFP signal frequency bands: Example signal and noise correlations across frequencies for a single LFP signal. Other channels demonstrated similar properties. Noise is mostly independent across frequencies, while the signal is encoded similarly across frequencies in certain bands. *A*: noise correlation significantly drops across frequencies that are spaced 10–20 Hz apart from each other. *B*: signal correlation stays high across certain frequencies bands, indicating that they encode signals similarly. Here, a position-velocity encoding model is shown (see METHODS for details) to demonstrate that LFP signals are modulated by velocity in addition to speed. Signal correlation was even higher when using a position-velocity- speed model. At *left* and *right*, the *1st row* and *column* represent the 1- to 10-Hz frequency band and the *last row* and *column* represent the 290- to 30-Hz frequency band.

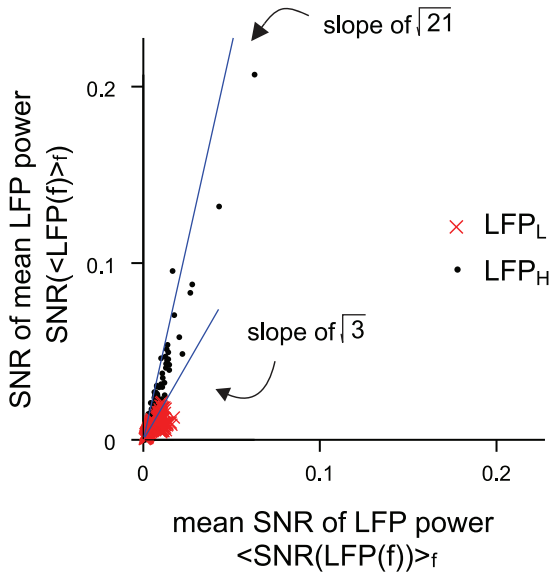

Fig. 13. Averaging LFP PSD across frequency bands increases signal to noise ratio: Each point corresponds to one electrode, and data from an entire recording session. Two sessions (1 from each monkey) are shown here. There are a total of 192 points for each of LFP_L and LFP_H. For the *x*-axis, we computed the SNR for every PSD frequency in LFP_L and LFP_H and then averaged the SNR values separately for the LFP_L and LFP_H frequencies. For the *y*-axis, we first averaged the LFP PSD across all frequencies in LFP_L or LFP_H, then computed the SNR for that LFP PSD frequency band. As expected from Fig. 12, averaging the LFP PSD first (*y*-axis) increases the signal to noise ratio. For the LFP_L frequency band, signal was weak, yet averaging provided slightly better SNR. For the LFP_H frequency band, averaging the LFP PSD first yielded much better SNR. The slopes of the lines are $\sqrt{3}$ and $\sqrt{21}$, which are the square roots of the number of frequencies in the LFP_L and LFP_H bands.

small fraction of channels (~20%), as indicated by the long whiskers in the box plots of Figs. 5 and 6.

We further evaluated the decay in noise and signal correlations as a function of distance across the cortical tissue under the recording array and, in the case of LFP, frequency within a single electrode. LFP_L showed a high correlation across the cortical tissue. At higher frequencies, LFP correlation decayed more sharply across the cortical tissue. TC activity shows relatively weak noise correlation even on neighboring electrodes, indicating a very local signal ($<$ 200-μm radius) source. In contrast, LFP showed a more gradual decline in noise correlation with distance: in the 50- to 100-Hz range, LFP noise correlations were still $>$0.2 even at the largest distances tested (~3 mm). We interpret these results to mean that these signal modalities convey information that is present at different spatial scales within the cortex.

A vast body of literature relates motor cortex SUA to various kinematic parameters during reaching movements (e.g., Georgopoulos et al. 1982; Scott and Kalaska 1995; Moran and Schwartz 1999; Churchland and Shenoy 2007; Kakei et al. 1999; Alexander and Crutcher 1990; Hatsopoulos et al. 2007; Paninski et al. 2004). Our results are in overall agreement with these findings. In particular, we see a prominent representation of velocity in SUA and a weaker representation of speed. There is heterogeneous encoding of all of the kinematic variables across our population, as evident by the long upper tails for the distributions in Fig. 6. Also in agreement with previous studies (e.g., Moran and Schwartz 1999), the average optimal lag between neural activity and kinematic variables was 100 ms (Fig. 4).

Different neural origins for different neural signal modalities. Movements are ultimately driven by action potentials conveying the collective activity of millions of cortical neurons. Voltage traces recorded using extracellular electrodes comprise a mixture of spiking activity and the postsynaptic potentials that give rise to spiking. We processed those voltage traces using two different nonlinear filters, the first to extract SUA/TC and the second to extract LFP (see Fig. 1). These two processing procedures provide us with two different, complementary views of the underlying neural process.

SUA activity, by definition, stems from the action of single neurons. TC signals likely reflect that activity of very local neurons, almost certainly numbering $<$10, given the thresholds used in this study. The source of the LFP signal is not yet agreed upon. Historically, LFPs have been considered to represent mainly synaptic activity and membrane-potential-derived voltage fluctuations (reviewed in Buzsáki et al. 2012). However, recent evidence suggests that spiking activity can affect the LFP power at all frequencies and that these effects cannot be simply removed by low-pass filtering the raw voltage signal (Waldert et al. 2013). We believe that our LFP_H signals included both spikes from local neurons and spikes from very distant neurons. The spatial scale of LFP signals is not well known and is likely to depend on frequency (Leopold et al. 2003; Einevoll et al. 2013). However, given that the 95th percentile of the R^2 distribution for velocity of the LFP_H signals is nearly half that of the TC signals (Fig. 6), it is likely that LFP_H integrates information over a substantially broader range than TC, sufficient to dilute the velocity tuning.

In addition to being tuned to movement direction, most neurons in motor cortex are also positively (albeit weakly) tuned to speed, meaning that increased movement speed will result in increased average firing rate (Moran and Schwartz 1999). However, the directional tuning of nearby neurons is only weakly correlated (Naselaris et al. 2006). Therefore, as signals from multiple neurons are combined (as is the case for TC and LFP_H), directional tuning should weaken while speed tuning strengthens. Indeed, we found that LFP_H signals encoded mostly speed information, with the exception of a subset of channels that also encode directional information. LFP_H PDs were most correlated with TC PDs, suggesting that LFP activity in the 100- to 300-Hz band contains some information from action potentials included in TC. LFP_H has both higher noise and signal correlations compared with TC, indicating that LFP_H signals are more homogeneous and tend to modulate similarly. TC signals recorded from two neighboring electrodes even just 400 μm apart have very low correlation. Our findings support the interpretation that SUA, TC, and LFP_H integrate information at increasing spatial scales within the cortex. Their neural origins are likely not identical: SUA is composed purely of spikes from one nearby neuron, TCs are probably a few neurons near the electrode tip, and also some more distant large neurons, with perhaps a contribution from postsynaptic potentials; LFP_H is probably a large-scale (approaching millimeters) aggregate of spiking activity and postsynaptic potentials; LFP_L is probably a generalized signal shared across a large swath of cortical tissue, far larger in spatial scale than our array could sample and perhaps also with a subcortical component. These interpretations are consistent with the trends in our data, although other explanations may

also fit the data, and verifying these interpretations is well beyond the scope of this work.

It is known that the beta band of LFP activity (here, LFP_L), roughly between 10 and 40 Hz, is suppressed during movement (Rickert et al. 2005). We confirmed this in our data. However, when assessing the encoding of kinematic features during a reach, at 100-ms resolution, we find that the moment-by-moment LFP_L activity is not well correlated with the moment-by-moment kinematic parameters. The already relatively small R^2 values for speed that we observe in the LFP_L band further decrease when we window our data to include only those hand speeds that are >10% of the maximum speed of the reach (data not shown). Thus, while LFP_L can be used to distinguish intended movement epochs from nonmovement epochs (e.g., Hwang and Andersen 2013), it does not appear to be useful for inferring instantaneous features of the reach. This supports our view that LFP_L signals reflect a nonspecific signal that arises from a much broader or more distant neural origin than LFP_H.

Implications for BMI decoding. Our results have implications for BMIs, devices that use recorded neural signals to actuate some device, such as a computer cursor (Taylor et al. 2002; Suminski et al. 2009; Ganguly and Carmena 2009; Hochberg et al. 2006; Mulliken et al. 2008; Schalk et al. 2007; Gilja et al. 2012; Ifft et al. 2013), robotic arm (Collinger et al. 2013; Hochberg et al. 2012; Wang et al. 2013), or muscle stimulator (Ethier et al. 2012; Moritz et al. 2008). TC activity is often thought to convey similar information as SUA. Several researchers have used TCs in place of SUA during BMI tasks (Santhanam et al. 2004; Fraser et al. 2009; Chestek et al. 2011; Sadtler et al. 2011; Hochberg et al. 2012; Christie et al. 2014). The general conclusion from that work has been that decoding performance can be just as good with TCs as with SUA. We find that although velocity encoding models fit to TC and SUA span a similar range of R^2 values (Figs. 5 and 6), there is more prominent speed encoding in our TC signals compared with SUA. In fact, it is in part because of this that TC signals encode information more similarly to LFP_H than to SUA. This indicates an avenue to improving BMI design: velocity information could be extracted from SUA, and TC could provide speed information. We note that it is likely that the prominent speed tuning we see also depends on our choice of threshold, which was set to be three times the root mean square value of the intertrial band-pass-filtered voltage trace. This is slightly more inclusive than is used in many BMI settings (e.g., Hochberg et al. 2012 and Chestek et al. 2011 used a setting of 4.5 times root mean square). Because of this, the speed tuning in TC in those studies may be somewhat less pronounced than it was in our data.

While the majority of BMIs rely on either sorted spikes or TC activity, there is an increasing recognition that LFP activity also carries useful information and may actually provide a more stable long-term signal for clinical applications (Flint et al. 2013; Markowitz et al. 2011; Bansal et al. 2012; Hwang and Andersen 2013).

Although it is sometimes dangerous to draw conclusions about online decoding performance from offline data (Chase et al. 2009; Cunningham et al. 2011), the prominent speed tuning we observe in our TC and LFP_H signals suggests that decoders that utilize these signal types would likely benefit from taking speed tuning into account. Unfortunately, since speed is a nonlinear transform of velocity, this implies that linear decoders such as the Kalman filter (Wu and Hatsopoulos 2008) may not actually be optimal when based on TC or LFP_H inputs. However, nonlinear state-space algorithms abound and have proven fruitful in decoding applications (e.g., Koyama et al. 2010; Li et al. 2009; Brockwell et al. 2004; Shpigelman et al. 2008; Dethier et al. 2013). Another approach to accounting for speed in improving BMI control would be to treat it as a "nuisance variable," and use latent variable approaches to mitigate its effect on decoding (Lawhern et al. 2010; Paninski et al. 2010). Speed control, especially in terms of stopping stability, is known to be poor in BMI control (Carmena et al. 2003; Hochberg et al. 2006; Kim et al. 2006; Ganguly and Carmena 2009; Gilja et al. 2012; Golub et al. 2014). It is possible that speed and stability could be improved by the addition of LFP_H and LFP_L signals to existing decoding algorithms.

Given the differential encoding of reach kinematics across the three signal types, we suggest that a hybrid approach may prove optimal for BMI decoding. This approach could rely more on the well-isolated single units to infer direction and more on the LFP_H signals to infer speed. The LFP_L signals could serve as an on/off switch to initiate movement. In a hybrid decoding scheme, SUA would be used whenever well-isolated neurons were available, and TC could be taken from the other electrodes. Together, they could provide direction and velocity information. LFP_H could provide speed information. Since LFP_H is so similar across electrodes, only a few electrodes would be needed. Of course, the same electrodes could be processed differently (Fig. 1) to attain signals of different modalities. Then, a signal to turn on and off neural control of the device could be taken from LFP_L (again, a few channels would be sufficient). In this way, a BMI could be designed that provides continuous use, eventually allowing such devices to be used outside of the laboratory setting.

GRANTS

Funding was provided by National Institute of Child Health and Human Development "Collaborative Research in Computational Neuroscience" Grant 5R01-HD-071686, National Institute of Neurological Disorders and Stroke Grant 5R01-NS-065065, the Burroughs Wellcome Fund, the Craig A. Neilsen Foundation, the DARPA Reliable Cortical Interfaces (RCI) Program, and the Pennsylvania Department of Health Research Formula Grant SAP#4100057653 under the Commonwealth Universal Research Enhancement Program.

DISCLOSURES

No conflicts of interest, financial or otherwise, are declared by the author(s).

AUTHOR CONTRIBUTIONS

Author contributions: S.P., P.T.S., E.R.O., A.P.B., and S.M.C. conception and design of research; S.P. analyzed data; S.P., E.R.O., A.P.B., and S.M.C. interpreted results of experiments; S.P. prepared figures; S.P., A.P.B., and S.M.C. drafted manuscript; S.P., P.T.S., E.R.O., S.I.R., E.C.T.-K., A.P.B., and S.M.C. edited and revised manuscript; S.P., P.T.S., E.R.O., S.I.R., E.C.T.-K., A.P.B., and S.M.C. approved final version of manuscript; P.T.S., S.I.R., and E.C.T.-K. performed experiments.

REFERENCES

Alexander GE, Crutcher MD. Preparation for movement: neural representations of intended direction in three motor areas of the monkey. *J Neurophysiol* 64: 133–150, 1990.

Asher I, Stark E, Abeles M, Prut Y. Comparison of direction and object selectivity of local field potentials and single units in macaque posterior parietal cortex during prehension. *J Neurophysiol* 97: 3684–3695, 2007.

Bansal AK, Truccolo W, Vargas-Irwin CE, Donoghue JP. Decoding 3D reach and grasp from hybrid signals in motor and premotor cortices: spikes, multiunit activity, and local field potentials. *J Neurophysiol* 107: 1337–1355, 2012.

Bansal AK, Vargas-Irwin CE, Truccolo W, Donoghue JP. Relationships among low-frequency local field potentials, spiking activity, and three-dimensional reach and grasp kinematics in primary motor and ventral premotor cortices. *J Neurophysiol* 105: 1603–1619, 2011.

Berger H. Hans Berger on the electroencephalogram of man (in German). *Arch F Psychiatr* 87: 527–570, 1929.

Brockwell AE, Rojas AL, Kass RE. Recursive Bayesian decoding of motor cortical signals by particle filtering. *J Neurophysiol* 91: 1899–1907, 2004.

Burton JE, Onoda N. Dependence of the activity of interpositus and red nucleus neurons on sensory input data generated by movement. *Brain Res* 152: 41–63, 1978.

Buzsáki G, Anastassiou CA, Koch C. The origin of extracellular fields and currents-EEG, ECOG, LFP and spikes. *Nat Rev Neurosci* 13: 407–420, 2012.

Carmena JM, Lebedev MA, Crist RE, O'Doherty JE, Santucci DM, Dimitrov DF, Patil PG, Henriquez CS, Nicolelis MA. Learning to control a brain-machine interface for reaching and grasping by primates. *PLoS Biol* 1: E42, 2003.

Chase SM, Schwartz AB, Kass RE. Bias, optimal linear estimation, and the differences between open-loop simulation and closed-loop performance of spiking-based brain-computer interface algorithms. *Neural Netw* 22: 1203–1213, 2009.

Chestek CA, Gilja V, Nuyujukian P, Foster JD, Fan JM, Kaufman MT, Churchland MM, Rivera-Alvidrez Z, Cunningham JP, Ryu SI. Long-term stability of neural prosthetic control signals from silicon cortical arrays in rhesus macaque motor cortex. *J Neural Eng* 8: 045005, 2011.

Christie BP, Tat DM, Irwin ZT, Gilja V, Nuyujukian P, Foster JD, Ryu SI, Shenoy KV, Thompson DE, Chestek CA. Comparison of spike sorting and thresholding of voltage waveforms for intracortical brain-machine interface performance. *J Neural Eng* 12: 016009, 2014.

Churchland MM, Shenoy KV. Temporal complexity and heterogeneity of single-neuron activity in premotor and motor cortex. *J Neurophysiol* 97: 4235–4257, 2007.

Collinger JL, Wodlinger B, Downey JE, Wang W, Tyler-Kabara EC, Weber DJ, McMorland AJ, Velliste M, Boninger ML, Schwartz AB. High-performance neuroprosthetic control by an individual with tetraplegia. *Lancet* 381: 557–564, 2013.

Cunningham JP, Nuyujukian P, Gilja V, Chestek CA, Ryu SI, Shenoy KV. A closed-loop human simulator for investigating the role of feedback control in brain-machine interfaces. *J Neurophysiol* 105: 1932–1949, 2011.

Dethier J, Nuyujukian P, Ryu SI, Shenoy KV, Boahen K. Design and validation of a real-time spiking-neural-network decoder for brain-machine interfaces. *J Neural Eng* 10: 036008, 2013.

Einevoll GT, Kayser C, Logothetis NK, Panzeri S. Modelling and analysis of local field potentials for studying the function of cortical circuits. *Nat Rev Neurosci* 14: 770–785, 2013.

Ethier C, Oby ER, Bauman MJ, Miller LE. Restoration of grasp following paralysis through brain-controlled stimulation of muscles. *Nature* 485: 368–371, 2012.

Flint RD, Lindberg EW, Jordan LR, Miller LE, Slutzky MW. Accurate decoding of reaching movements from field potentials in the absence of spikes. *J Neural Eng* 9: 046006, 2012.

Flint RD, Wright ZA, Scheid MR, Slutzky MW. Long term, stable brain machine interface performance using local field potentials and multiunit spikes. *J Neural Eng* 10: 056005, 2013.

Foster J, Freifeld O, Nuyujukian P, Ryu S, Black M, Shenoy K. Combining wireless neural recording and video capture for the analysis of natural gait. In: *2011 5th International IEEE/EMBS Conference on Neural Engineering (NER)*. New York: IEEE, 2011, p. 613–616.

Fraser GW, Chase SM, Whitford A, Schwartz AB. Control of a brain computer interface without spike sorting. *J Neural Eng* 6: 055004, 2009.

Fu QG, Flament D, Coltz JD, Ebner TJ. Temporal encoding of movement kinematics in the discharge of primate primary motor and premotor neurons. *J Neurophysiol* 73: 836–854, 1995.

Ganguly K, Carmena JM. Emergence of a stable cortical map for neuroprosthetic control. *PLoS Biol* 7: e1000153, 2009.

Georgopoulos AP, Kalaska JF, Caminiti R, Massey JT. On the relations between the direction of two-dimensional arm movements and cell discharge in primate motor cortex. *J Neurosci* 2: 1527–1537, 1982.

Georgopoulos AP, Schwartz AB, Kettner RE. Neuronal population coding of movement direction. *Science* 233: 1416–1419, 1986.

Gilja V, Nuyujukian P, Chestek CA, Cunningham JP, Yu BM, Fan JM, Churchland MM, Kaufman MT, Kao JC, Ryu SI, Shenoy KV. A high-performance neural prosthesis enabled by control algorithm design. *Nat Neurosci* 15: 1752–1757, 2012.

Golub MD, Yu BM, Schwartz AB, Chase SM. Motor cortical control of movement speed with implications for brain-machine interface control. *J Neurophysiol* 112: 411–429, 2014.

Hatsopoulos NG, Xu Q, Amit Y. Encoding of movement fragments in the motor cortex. *J Neurosci* 27: 5105–5114, 2007.

Heldman DA, Wang W, Chan SS, Moran DW. Local field potential spectral tuning in motor cortex during reaching. *IEEE Trans Neural Syst Rehabil Eng* 14: 180–183, 2006.

Hochberg LR, Bacher D, Jarosiewicz B, Masse NY, Simeral JD, Vogel J, Haddadin S, Liu J, Cash SS, van der Smagt P. Reach and grasp by people with tetraplegia using a neurally controlled robotic arm. *Nature* 485: 372–375, 2012.

Hochberg LR, Serruya MD, Friehs GM, Mukand JA, Saleh M, Caplan AH, Branner A, Chen D, Penn RD, Donoghue JP. Neuronal ensemble control of prosthetic devices by a human with tetraplegia. *Nature* 442: 164–171, 2006.

Hwang EJ, Andersen RA. The utility of multichannel local field potentials for brain-machine interfaces. *J Neural Eng* 10: 046005, 2013.

Ifft PJ, Shokur S, Li Z, Lebedev MA, Nicolelis MA. A brain-machine interface enables bimanual arm movements in monkeys. *Sci Transl Med* 5: 210ra154, 2013.

Insel TR, Landis SC, Collins FS. Research priorities. The NIH BRAIN initiative. *Science* 340: 687–688, 2013.

Kakei S, Hoffman DS, Strick PL. Muscle and movement representations in the primary motor cortex. *Science* 285: 2136–2139, 1999.

Kim SP, Sanchez JC, Rao YN, Erdogmus D, Carmena JM, Lebedev MA, Nicolelis MA, Principe JC. A comparison of optimal mimo linear and nonlinear models for brain-machine interfaces. *J Neural Eng* 3: 145–161, 2006.

Koyama S, Perez-Bolde LC, Shalizi CR, Kass RE. Approximate methods for state-space models. *J Am Stat Assoc* 105: 170–180, 2010.

Lawhern V, Wu W, Hatsopoulos N, Paninski L. Population decoding of motor cortical activity using a generalized linear model with hidden states. *J Neurosci Methods* 189: 267–280, 2010.

Leopold DA, Murayama Y, Logothetis NK. Very slow activity fluctuations in monkey visual cortex: implications for functional brain imaging. *Cereb Cortex* 13: 422–433, 2003.

Li Z, O'Doherty JE, Hanson TL, Lebedev MA, Henriquez CS, Nicolelis MA. Unscented Kalman filter for brain-machine interfaces. *PLoS One* 4: e6243, 2009.

Markowitz DA, Wong YT, Gray CM, Pesaran B. Optimizing the decoding of movement goals from local field potentials in macaque cortex. *J Neurosci* 31: 18412–18422, 2011.

Mehring C, Rickert J, Vaadia E, de Oliveira SC, Aertsen A, Rotter S. Inference of hand movements from local field potentials in monkey motor cortex. *Nat Neurosci* 6: 1253–1254, 2003.

Moran DW, Schwartz AB. Motor cortical representation of speed and direction during reaching. *J Neurophysiol* 82: 2676–2692, 1999.

Moritz CT, Perlmutter SI, Fetz EE. Direct control of paralysed muscles by cortical neurons. *Nature* 456: 639–642, 2008.

Mulliken GH, Musallam S, Andersen RA. Decoding trajectories from posterior parietal cortex ensembles. *J Neurosci* 28: 12913–12926, 2008.

Naselaris T, Merchant H, Amirikian B, Georgopoulos AP. Large-scale organization of preferred directions in the motor cortex. II. Analysis of local distributions. *J Neurophysiol* 96: 3237–3247, 2006.

Paninski L. Superlinear population encoding of dynamic hand trajectory in primary motor cortex. *J Neurosci* 24: 8551–8561, 2004.

Paninski L, Ahmadian Y, Ferreira DG, Koyama S, Rahnama Rad K, Vidne M, Vogelstein J, Wu W. A new look at state-space models for neural data. *J Comput Neurosci* 29: 107–126, 2010.

Paninski L, Fellows MR, Hatsopoulos NG, Donoghue JP. Spatiotemporal tuning of motor cortical neurons for hand position and velocity. *J Neurophysiol* 91: 515–532, 2004.

Rickert J, Oliveira SC, Vaadia E, Aertsen A, Rotter S, Mehring C. Encoding of movement direction in different frequency ranges of motor cortical local field potentials. *J Neurosci* 25: 8815–8824, 2005.

Riehle A, Vaadia E. *Motor Cortex in Voluntary Movements: a Distributed System for Distributed Functions. Frontiers in Neuroscience*. Boca Raton, FL: CRC, 2005.

Sadtler PT, Ryu SI, Yu B, Batista AP. High-performance neural prosthetic control along instructed paths. In: *2011 5th International IEEE/EMBS Conference on Neural Engineering (NER)*. New York: IEEE, 2011, p. 601–604.

Santhanam G, Sahani M, Ryu SI, Shenoy KV. An extensible infrastructure for fully automated spike sorting during online experiments. In: *Engineering in Medicine and Biology Society, 2004. IEMBS'04. 26th Annual International Conference of the IEEE*. New York: IEEE, 2004, vol. 2, p. 4380–4384, 2004.

Schalk G, Kubanek J, Miller KJ, Anderson NR, Leuthardt EC, Ojemann JG, Limbrick D, Moran D, Gerhardt LA, Wolpaw JR. Decoding two-dimensional movement trajectories using electrocorticographic signals in humans. *J Neural Eng* 4: 264–75, 2007.

Schalk G, McFarland DJ, Hinterberger T, Birbaumer N, Wolpaw JR. BCI2000: a general purpose brain-computer interface (BCI) system. *IEEE Trans Biomed Eng* 51: 1034–1043, 2004.

Schwarz DA, Lebedev MA, Hanson TL, Dimitrov DF, Lehew G, Meloy J, Rajangam S, Subramanian V, Ifft PJ, Li Z, Ramakrishnan A, Tate A, Zhuang KZ, Nicolelis MA. Chronic, wireless recordings of large-scale brain activity in freely moving Rhesus monkeys. *Nat Methods* 11: 67067–67066, 2014.

Scott SH, Kalaska JF. Changes in motor cortex activity during reaching movements with similar hand paths but different arm postures. *J Neurophysiol* 73: 2563–2567, 1995.

Shpigelman L, Lalazar H, Vaadia E. Kernel-ARMA for hand tracking and brain-machine interfacing during 3D motor control. In: *Advances in Neural Information Processing Systems 21 (NIPS 2008)*. Vancouver, Canada: NIPS, 208, p. 1489–1496.

Soechting JF, Burton JE, Onoda N. Relationships between sensory input, motor output and unit activity in interpositus and red nuclei during intentional movement. *Brain Res* 152: 65–79, 1978.

Stark E, Abeles M. Predicting movement from multiunit activity. *J Neurosci* 27: 8387–8394, 2007.

Stevenson IH, Kording KP. How advances in neural recording affect data analysis. *Nat Neurosci* 14: 139–142, 2011.

Suminski AJ, Tkach DC, Hatsopoulos NG. Exploiting multiple sensory modalities in brain-machine interfaces. *Neural Netw* 22: 1224–1234, 2009.

Taylor DM, Tillery SI, Schwartz AB. Direct cortical control of 3D neuroprosthetic devices. *Science* 296: 1829–1832, 2002.

Viviani P, Terzuolo CA. Modeling of a simple motor task in man: intentional arrest of an ongoing movement. *Kybernetik* 14: 35–62, 1973.

Waldert S, Lemon RN, Kraskov A. Influence of spiking activity on cortical local field potentials. *J Physiol* 591: 5291–5303, 2013.

Wang W, Collinger JL, Degenhart AD, Tyler-Kabara EC, Schwartz AB, Moran DW, Weber DJ, Wodlinger B, Vinjamuri RK, Ashmore RC, Kelly JW, Boninger ML. An electrocorticographic brain interface in an individual with tetraplegia. *PLoS One* 8: e55344, 2013.

Wu W, Hatsopoulos NG. Real-time decoding of nonstationary neural activity in motor cortex. *IEEE Trans Neural Syst Rehabil Eng* 16: 213–222, 2008.

Zhuang J, Truccolo W, Vargas-Irwin C, Donoghue JP. Decoding 3-D reach and grasp kinematics from high-frequency local field potentials in primate primary motor cortex. *IEEE Trans Biomed Eng* 57: 1774–1784, 2010a.

Zhuang J, Truccolo W, Vargas-Irwin C, Donoghue JP. Reconstructing grasping motions from high-frequency local field potentials in primary motor cortex. *Conf Proc IEEE Eng Med Biol Soc* 2010: 4347–4350, 2010b.